

Cite this article as: Huang Ting, Liu Huiqun, Lin Gaoyong, et al. Microstructure and Mechanical Properties of Ultra-high Strength Al-7.88Zn-2.05Mg-1.70Cu-0.19Er Aluminum Alloy Thin Strip[J]. Rare Metal Materials and Engineering, 2022, 51(09): 3189-3196.

ARTICLE

# Microstructure and Mechanical Properties of Ultra-high Strength Al-7.88Zn-2.05Mg-1.70Cu-0.19Er Aluminum Alloy Thin Strip

Huang Ting<sup>1</sup>, Liu Huiqun<sup>1</sup>, Lin Gaoyong<sup>1</sup>, Zheng Ying<sup>2</sup>

<sup>1</sup> School of Materials Science and Engineering, Central South University, Changsha 410083, China; <sup>2</sup> Light Alloy Research Institute, Central South University, Changsha 410083, China

**Abstract:** The microstructure, mechanical properties, and corrosion resistance of ultra-high strength cold-rolled thin strips of Al-7.88Zn-2.05Mg-1.70Cu-0.19Er alloy were investigated. Results reveal that the excellent comprehensive properties of the cold-rolled thin strips with 0.5 mm in thickness are achieved after solid solution treatment of 475 °C/1 h/water quenching and double aging treatment of 120 °C/6 h+150 °C/24 h. The hardness, ultimate tensile strength, yield strength, and elongation of the thin strips are 1859.1 MPa, 669.4 MPa, 624.1 MPa, and 11.2%, respectively. The mechanical properties of double-aged strip are comparable to those of alloy after peak-aging treatment. The electrical conductivity, exfoliation corrosion rating, and stress corrosion cracking sensitivity of the thin strip are 35.5%IACS, EA, and 4.07%, respectively. The fine spherical Al<sub>3</sub>(Er, Zr) and η' phases are uniformly distributed in the Al matrix, and most precipitates are coherent with Al matrix lattice. The tiny discontinuous grain boundary precipitate η phase mainly causes the lower stress corrosion sensitivity of the studied alloy.

**Key words:** Al-7.88Zn-2.05Mg-1.70Cu-0.19Er alloy; thin strip; double aging; mechanical properties; corrosion resistance

The ultra-high strength aluminum alloy thin strips have great application potential in automobile, rail transit, aerospace, and engineering equipment fields owing to their lightweight<sup>[1,2]</sup>. The ultra-high strength thin strips can replace 6XXX and 5XXX series aluminum alloy strips in shell and panel processing, significantly improving the bearing capacity and reducing the mass of products. However, the applications of 7XXX series alloy thin sheets are restricted by the poor plasticity and inferior toughness<sup>[3]</sup>. Additionally, the ultra-high strength Al-Zn-Mg-Cu alloys are susceptible to stress corrosion cracking (SCC), which leads to failure<sup>[4]</sup>.

Excellent mechanical properties and stress corrosion resistance are hard to achieve simultaneously for Al-Zn-Mg-Cu alloys. The micro-alloying is one of the effective methods to optimize the comprehensive properties of alloys<sup>[3-5]</sup>. It is found that a trace amount of Er addition can effectively purify the melt, refine the grain, and reduce the coarse brittle phase, resulting in superior cold and hot deformation ability<sup>[6-8]</sup>. Fang

et al<sup>[9]</sup> suggested that adding Er into the Al-Cu-Mg alloy improves the intergranular corrosion resistance. Besides, Er addition induces the formation of Al<sub>3</sub>Er phase, which refines the grains during recrystallization, and the continuous η phase at the grain boundary is transformed into the discontinuous phase during subsequent aging treatment<sup>[10,11]</sup>.

Al-Zn-Mg-Cu alloy is an ultra-high strength aluminum alloy strengthened by heat treatment<sup>[12,13]</sup>. The heat treatment changes not only the morphology, size, and distribution of the precipitated phases in matrix, but also the structure and morphology of precipitates at grain boundaries<sup>[14-16]</sup>. Therefore, the aging treatment can significantly affect the stress corrosion resistance. Pan et al<sup>[16]</sup> demonstrated that different aging-induced precipitates have different influences on the stress corrosion behavior of 7050 aluminum alloys. Chen et al<sup>[17]</sup> found that the highly continuous distribution of grain boundary precipitates (GBPs) promotes the continuous propagation of stress crack along the grain boundary, leading

Received date: September 10, 2021

Foundation item: National Natural Science Foundation of China (51274245)

Corresponding author: Lin Gaoyong, Ph. D., Professor, School of Materials Science and Engineering, Central South University, Changsha 410083, P. R. China, E-mail: gylin6609@csu.edu.cn

Copyright © 2022, Northwest Institute for Nonferrous Metal Research. Published by Science Press. All rights reserved.

to intergranular SCC. In addition, the discontinuously distributed coarse GBPs can hinder anodic dissolution along the grain boundary, and the large size and low density of matrix precipitates (MPTs) can decrease the SCC sensitivity.

Currently, the studies on cold-rolled ultra-high strength aluminum alloy thin strip are rarely conducted. The main processing techniques of ultra-high-strength aluminum alloy plates are hot rolling and extrusion, whereas the cold rolling is rarely used to produce thin slabs with thickness of 1 mm<sup>[18,19]</sup>. In this research, a novel aluminum alloy, Al-7.88Zn-2.05Mg-1.70Cu-0.19Er alloy, was used for investigation<sup>[20]</sup>. After solution treatment of 475 °C/1 h, different aging processes were conducted for the alloy to study the mechanical properties and microstructure evolution of Al-7.88Zn-2.05Mg-1.70Cu-0.19Er thin strip, which provides theoretical basis for the heat treatment design.

## 1 Experiment

The commercially hot-rolled Al-7.88Zn-2.05Mg-1.70Cu-0.19Er alloy strip with thickness of 3.5 mm was used in this research. The actual chemical composition of the alloy strip is shown in Table 1. The hot-rolled plate was annealed at 380 °C for 3 h in box-type crucible electric furnace, and then furnace-cooled to 100 °C. Finally, the thin strip of 0.5 mm in thickness was obtained after 4 passes of cold rolling.

The cold-rolled specimens were solution-treated at 475 °C for 1 h, and then quenched immediately in cold water (transfer time < 5 s). Subsequently, three aging treatments (peak-aging, over-aging, double-aging) were conducted for the specimens, as shown in Table 2.

The Vickers hardness of specimens was tested using Vickers hardness tester (HVS-1000) at load of 0.3 kg with loading time of 10 s. The electrical conductivity was measured by an eddy current conductor meter (D60K), and the standard blocks were used to calibrate before measuring.

The uniaxial tensile tests were conducted at room temperature by electronic universal material testing machine (Instron3369) at tensile speed of 2 mm/min. The tensile specimens were cut from the thin strip along the rolling direction with the size of 25 mm×8 mm.

According to HB 7235-1995 standard, the slow strain rate testing (SSRT) was conducted in dry air and 3.5wt% NaCl solution (pH=8) with strain rate of  $1.0 \times 10^{-6} \text{ s}^{-1}$ , and the

**Table 1 Chemical composition of Al-7.88Zn-2.05Mg-1.70Cu-0.19Er alloy strip (wt%)**

Zn	Mg	Cu	Fe	Er	Zr	Ca	Al
7.88	2.05	1.70	0.64	0.19	0.16	0.13	Bal.

**Table 2 Processing conditions of different aging treatments**

Aging treatment	Processing condition
Peak-aging	120 °C/24 h
Over-aging	160 °C/24 h
Double-aging	120 °C/6 h+150 °C/24 h

schematic diagram of SSRT specimen is shown in Fig. 1. According to GB-T 22639-2008 standard, the specimens were immersed in exfoliation corrosion (EXCO) solution (234 g NaCl+50 g KNO<sub>3</sub>+6.3 mL HNO<sub>3</sub>+distilled water with total solution volume of 1000 mL) at 25 °C for 48 h.

The specimens for optical microscope (OM) observation were ground, polished, and etched by Keller's reagent (2 mL HF+3 mL HCl+5 mL HNO<sub>3</sub>+95 mL H<sub>2</sub>O). The cross-section morphologies of the specimens were analyzed by electron backscattered diffraction (EBSD). The EBSD specimens were prepared by electropolishing with 10vol% perchloric acid and 90vol% ethanol before examination. In this research, the Channel 5 software was used to calculate the grain size, misorientation, and recrystallization of Al-7.88Zn-2.05Mg-1.70Cu-0.19Er alloy strip. The GBPs, precipitate free zone (PFZ), and MPTs of the specimens were observed by transmission electron microscope (TEM, Talos F200X) operated at 200 kV. The thin foils prepared for TEM observation were mechanically ground to 70 μm in thickness, punched into 3 mm in diameter, and then twin-jet electropolished by the solution of 25vol% HNO<sub>3</sub>+75vol% CH<sub>3</sub>OH at -30 °C.

## 2 Results and Discussion

### 2.1 Microstructure of solution-treated alloy

The cold-rolled thin strip was solution-treated at 475 °C for 1 h and then water-quenched into room temperature. Fig. 2a shows OM microstructures of the thin strip along three principal directions: normal direction (ND), transverse direction (TD), and rolling direction (RD). The grains along ND, RD, and TD are equiaxed, lath-shaped, and needle-shaped, respectively. EBSD mapping in Fig. 2b shows that the solution-treated alloy strip contains fine subgrains. According to Fig. 2c and 2d, the incompletely recrystallized grains exist due to the formation of Al<sub>3</sub>(Er, Zr) phase, which significantly inhibits the recrystallization of Al matrix, maintaining the numerous fine substructures<sup>[4]</sup>. The recrystallization area fraction accounts for 50.83%. Fig. 2e indicates that the low angle grain boundaries (<15°) account for 27.8% in the solution-treated thin strip. The grain size of 7055 aluminum alloy is generally 30~35 μm<sup>[19,21]</sup>. Fig. 2f indicates that the grains in this alloy strip are tiny with the average grain size of 15.53 μm.

### 2.2 Hardness and electrical conductivity

Fig. 3 shows the hardness and electrical conductivity of the Al-7.88Zn-2.05Mg-1.70Cu-0.19Er alloy strips after different aging treatments. The hardness and electrical conductivity of peak-aged alloy are 1862.0 MPa and 32.0%IACS,

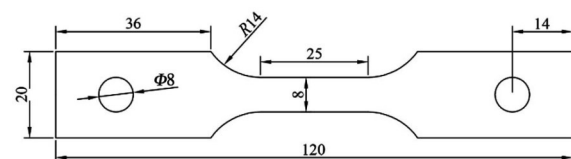


Fig.1 Schematic diagram of tensile specimen

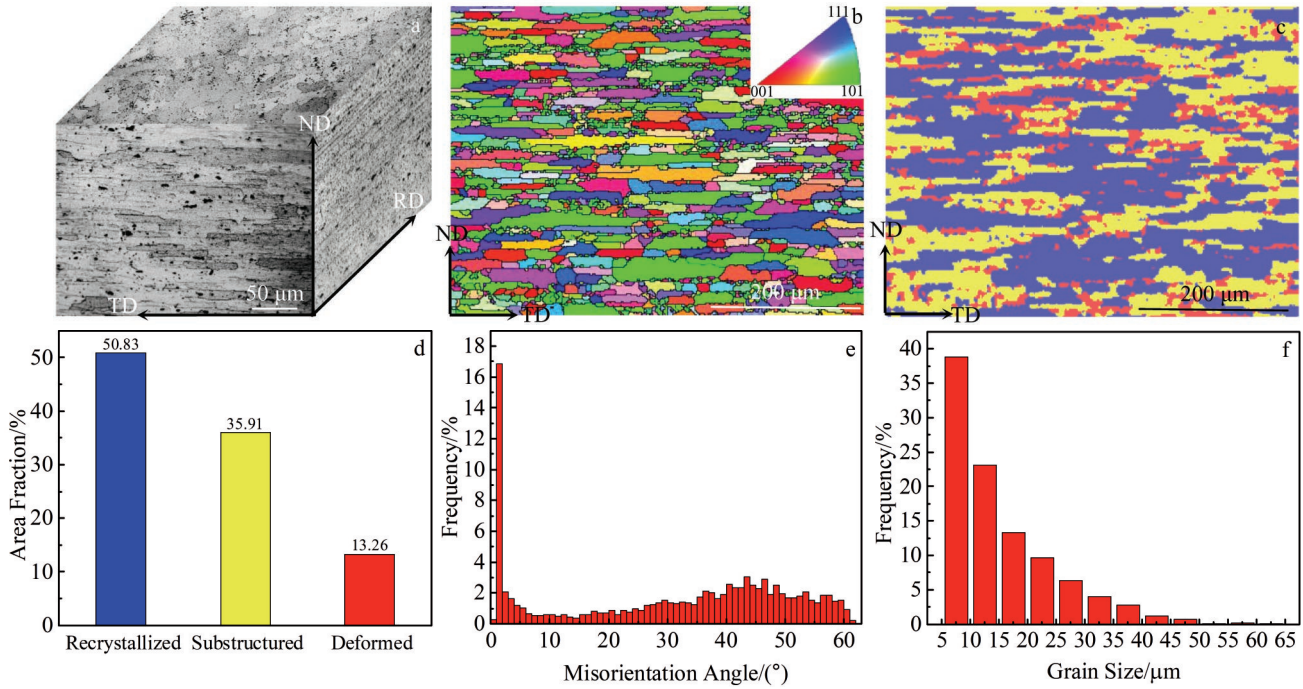


Fig.2 OM microstructures (a) and EBSD analyses results (b~f) of Al-7.88Zn-2.05Mg-1.70Cu-0.19Er alloy after solution treatment: (b) grain structure, (c) recrystallization distribution, (d) proportion of different grains, (e) grain boundary misorientation, and (f) grain size distribution

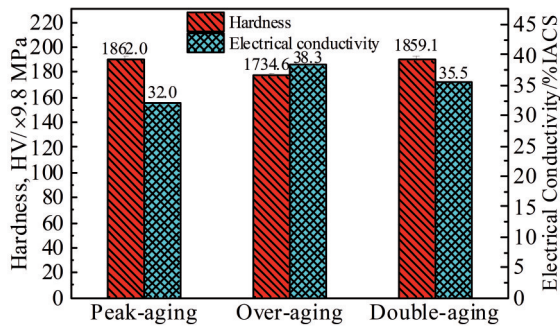


Fig.3 Hardness and electrical conductivity of Al-7.88Zn-2.05Mg-1.70Cu-0.19Er alloys after different aging treatments

respectively. It is known that the hardness of alloy after peak-aging treatment is normally higher than that of others. Compared with that of the alloys after over-aging and double-aging treatments, the electrical conductivity of the peak-aged alloy is the lowest. The electrical conductivity of the alloy after over-aging increases to 38.3% IACS, while its hardness is 127.4 MPa lower than that after peak-aging. It is worth noting that the hardness of the alloy after double-aging treatment (1859.1 MPa) is basically the same as that of the peak-aged alloy, and its electrical conductivity is only 2.8% IACS lower than that of the over-aged alloy.

Generally, the hardness is approximately proportional to the tensile strength of alloys<sup>[22]</sup>. Besides, the higher the electrical conductivity, the better the stress corrosion resistance of the material<sup>[23]</sup>. In conclusion, the aging treatment of 120 °C/6 h+

150 °C/24 h is optimal for Al-7.88Zn-2.05Mg-1.70Cu-0.19Er alloy to obtain the optimum comprehensive mechanical properties.

### 2.3 Tensile properties

The tensile properties of Al-7.88Zn-2.05Mg-1.70Cu-0.19Er alloy after different aging treatments are shown in Fig.4. The ultimate tensile strength (UTS), yield strength (YS), and elongation (EL) of the peak-aged alloy are 671.9 MPa, 634.1 MPa, and 6.4%, respectively. UTS and YS of over-aged alloy decrease by 81.6 and 78.4 MPa, compared with those of peak-aged alloy, respectively, whereas its EL increases to 11.8%. However, compared with those of peak-aged alloy, UTS and YS of the double-aged alloy only decrease by 2.5 and 10.0 MPa, respectively, and its EL increases to 11.2%. Therefore, the over-aging treatment can greatly improve the plasticity of

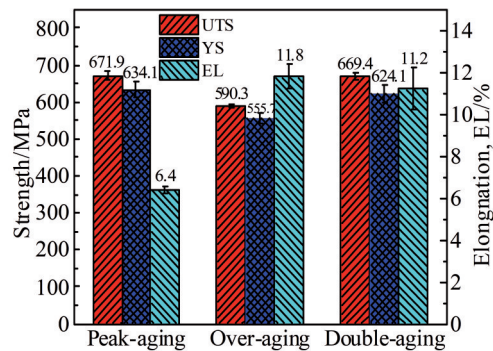


Fig.4 Tensile properties of Al-7.88Zn-2.05Mg-1.70Cu-0.19Er alloy after different aging treatments

peak-aged alloy, but reduce UTS and YS obviously. The hardness, UTS, YS, and EL of alloy after double-aging treatment are 1859.1 MPa, 669.4 MPa, 624.1 MPa, and 11.2%, respectively. Therefore, the double-aging treatment can optimize the comprehensive mechanical properties of Al-7.88Zn-2.05Mg-1.70Cu-0.19Er alloy.

#### 2.4 SCC sensitivity and fracture morphologies

SSRT was conducted to investigate the SCC sensitivity of alloy ( $I_{SSRT}$ ), and its expression<sup>[24]</sup> is as follows:

$$I_{SSRT} = \left[ 1 - \frac{\sigma_{fw}(1 + \delta_{fw})}{\sigma_{fa}(1 + \delta_{fa})} \right] \times 100\% \quad (1)$$

where  $\sigma_{fw}$  is the fracture strength in environmental media;  $\sigma_{fa}$  is the fracture strength in inert media;  $\delta_{fw}$  is the elongation in environmental media;  $\delta_{fa}$  is the elongation in inert media. The larger the value of  $I_{SSRT}$ , the more obvious the SCC sensitivity.

The stress-strain curves of the three specimens under different heat-treatments during SSRT are displayed in Fig. 5, and the experiment results are shown in Table 3. According to Fig. 5, compared with those in dry air, the strength and elongation of each specimen in 3.5wt% NaCl solution decrease significantly, indicating that the stress corrosion of the alloy specimens is severe in 3.5wt% NaCl solution.

According to Table 3,  $I_{SSRT}$  values of the alloys after peak-aging, over-aging, and double-aging are 4.96%, 3.56%, and 4.07%, respectively. The stress corrosion sensitivity of peak-aged alloy is the highest, which is consistent with the large loss of fracture strength and elongation in corrosive environment, compared with those of peak-aged alloy in dry air. Although the elongation decreases obviously and the fracture strength increases slightly for over-aged alloy, its  $I_{SSRT}$

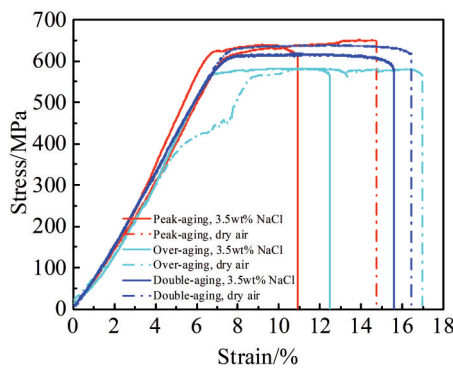


Fig.5 Stress-strain curves of Al-7.88Zn-2.05Mg-1.70Cu-0.19Er alloys after different aging treatments in dry air and 3.5wt% NaCl solution

is the smallest among these specimens. Thus, considering the stress corrosion resistance, the over-aging is the optimal heat treatment for Al-7.88Zn-2.05Mg-1.70Cu-0.19Er alloy.

After SSRT in dry air and 3.5wt% NaCl solution, the fracture morphologies of specimens were analyzed, as shown in Fig. 6. The white rectangular areas are magnified, as shown in the insets of Fig. 6. The fracture morphologies of alloy specimens in dry air are similar to those in 3.5wt% NaCl solution. As shown in Fig. 6a and 6b, the intergranular fractures can be observed at the edge of peak-aged alloy, as well as the transgranular cleavage fracture. The fracture morphologies of over-aged alloy in both corrosive environments show transgranular dimple fractures (Fig. 6c and 6d). Fig. 6e and 6f demonstrate that the double-aged alloys in both corrosive environments have the intergranular dimple fracture morphology.

#### 2.5 EXCO

Fig. 7 presents EXCO morphologies of the Al-7.88Zn-2.05Mg-1.70Cu-0.19Er alloys after different heat treatments. It can be seen that all alloys suffer severe EXCO. According to evaluation standard, the EXCO rating of the alloys after peak-aging, over-aging, and double-aging treatments is EC, EA, and EB, respectively. The peak-aged alloy specimen has the worst EXCO rating (Fig. 7a), because the blisters and delamination can be observed on the specimen surface. In contrast, the size and number of blisters are obviously decreased and less delamination occurs on the specimen surfaces of alloys after over-aging and double-aging treatments, as shown in Fig. 7b and 7c. Particularly, the EXCO sensitivity is significantly improved by over-aging treatment. Therefore, the order of enhancement effect of aging treatments on EXCO resistance is peak-aging < double-aging < over-aging.

Fig. 8 shows the corrosion depths of Al-7.88Zn-2.05Mg-1.70Cu-0.19Er alloys after different treatments. The minimum corrosion depth is 59.4  $\mu\text{m}$  in the over-aged alloy specimen, as shown in Fig. 8b. The maximum depth of 90.3  $\mu\text{m}$  is obtained in the peak-aged alloy specimen, as shown in Fig. 8a. The corrosion depth of double-aged alloy specimen is 72.1  $\mu\text{m}$ .

#### 2.6 Precipitates

The high-angular annular dark-field detector in scanning transmission electron microscope (HAADF-STEM) and selected area electron diffraction (SAED) were used to analyze the precipitates in Al-7.88Zn-2.05Mg-1.70Cu-0.19Er alloys after different heat treatments. Fig. 9 presents HAADF-

Table 3 SSRT results of Al-7.88Zn-2.05Mg-1.70Cu-0.19Er alloys after different aging treatments

Treatment	Environmental medium	Fracture strength, $\sigma_f$ /MPa	Elongation, $\delta$ /%	$I_{SSRT}$ /%
Peak-aging	3.5wt% NaCl solution	639.8	10.9	4.96
	Dry air	650.9	14.7	
Over-aging	3.5wt% NaCl solution	582.6	12.5	3.56
	Dry air	580.9	17.0	
Double-aging	3.5wt% NaCl solution	619.4	15.6	4.07
	Dry air	639.8	16.5	

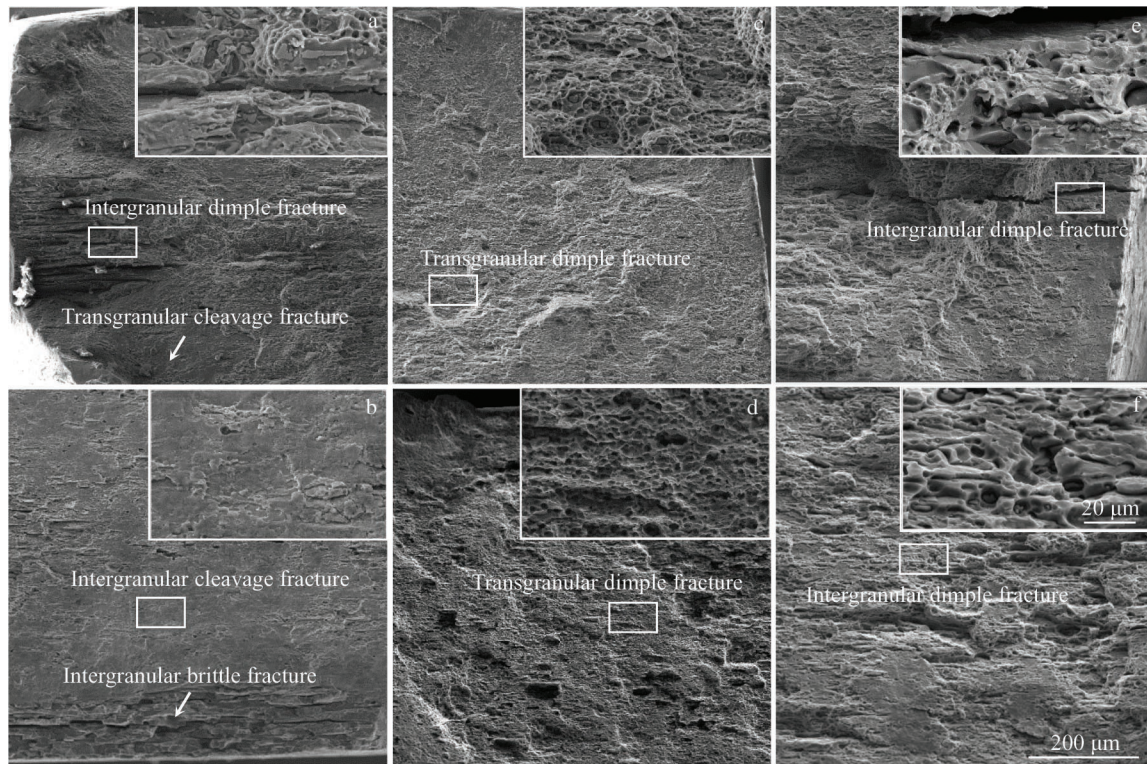


Fig.6 SEM fracture morphologies of peak-aged (a, b), over-aged (c, d), and double-aged (e, f) Al-7.88Zn-2.05Mg-1.70Cu-0.19Er alloys after SSRT in dry air (a, c, e) and 3.5wt% NaCl solution (b, d, f)



Fig.7 EXCO morphologies of Al-7.88Zn-2.05Mg-1.70Cu-0.19Er alloys after peak-aging (a), over-aging (b), and double-aging (c) treatments

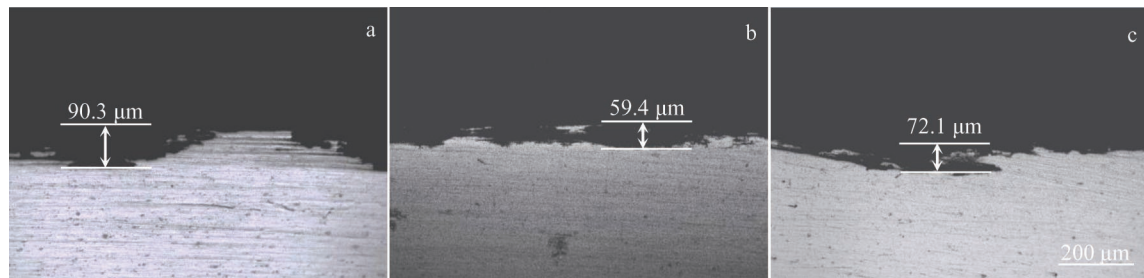


Fig.8 Corrosion depths of Al-7.88Zn-2.05Mg-1.70Cu-0.19Er alloys after peak-aging (a), over-aging (b), and double-aging (c) treatments

STEM morphologies, SAED patterns, and high-resolution TEM (HRTEM) images of Al-7.88Zn-2.05Mg-1.70Cu-0.19Er

alloys after different heat treatments along the  $\langle 011 \rangle_{Al}$  zone axis. Because the intensity depends on atomic number, the

bright contrast indicates the large atomic number, which corresponds to Cu or Zn atoms. In the peak-aged alloy specimen (Fig. 9a), a large number of fine precipitates and some coarser spherical precipitates are homogeneously distributed in Al matrix. However, only the diffraction spots of  $\eta$  phase parallel to  $\{220\}_{\text{Al}}$  can be observed in Fig. 9d. The  $\text{Al}_3(\text{Er, Zr})$  and  $\eta'$  precipitate phases are too small to be detected. Fig. 9g suggests that most precipitates are coherent with Al matrix lattice, which illustrates that the alloy elements still dissolve in Al matrix, and the tiny spherical  $\text{Al}_3(\text{Er, Zr})$  phase of 4.2 nm in size,  $\eta'$  phase (indicated by yellow arrows in Fig. 9), and stacking fault (SF) are also distributed in Al matrix. The  $\text{Al}_3(\text{Er, Zr})$  and  $\eta'$  phases can be identified through the fast Fourier transform (FFT) pattern along  $\langle 011 \rangle_{\text{Al}}$  in the inset of Fig. 9g.

As shown in Fig. 9b, the coarse precipitates and tiny white spherical  $\text{Al}_3(\text{Er, Zr})$  phase of 4.9 nm in size are uniformly

distributed in matrix.  $\text{Al}_3(\text{Er, Zr})$  phases are marked by the dotted square areas in Fig. 9. According to Zener formula<sup>[25]</sup>, the larger the particle size, the worse the blocking effect against dislocation. Therefore, the strength of over-aged alloy decreases obviously, which is consistent with the tensile test results. In addition, the  $\text{Al}_3(\text{Er, Zr})$ ,  $\eta'$ , and  $\eta$  phases can be observed in Fig. 9e. Fig. 9h shows that the coarse precipitates, which are incoherent with Al matrix lattice, are obvious, suggesting that the alloy elements are separated from Al matrix. According to the insets of FFT patterns in Fig. 9h, Guinier Preston (GP) zones parallel to  $1/2(311)$  and awn line are generated by SF, which is about 17.7 nm. SF elongates the reciprocal point, which is corresponding to the  $\{111\}$  plane, along  $\langle 111 \rangle$  direction into reciprocal rod, thus forming diffraction awn line. The direction of awn line is related to SF direction. Compared with that of the peak-aged alloy, the plasticity of over-aged alloy is improved by SF. SFs can

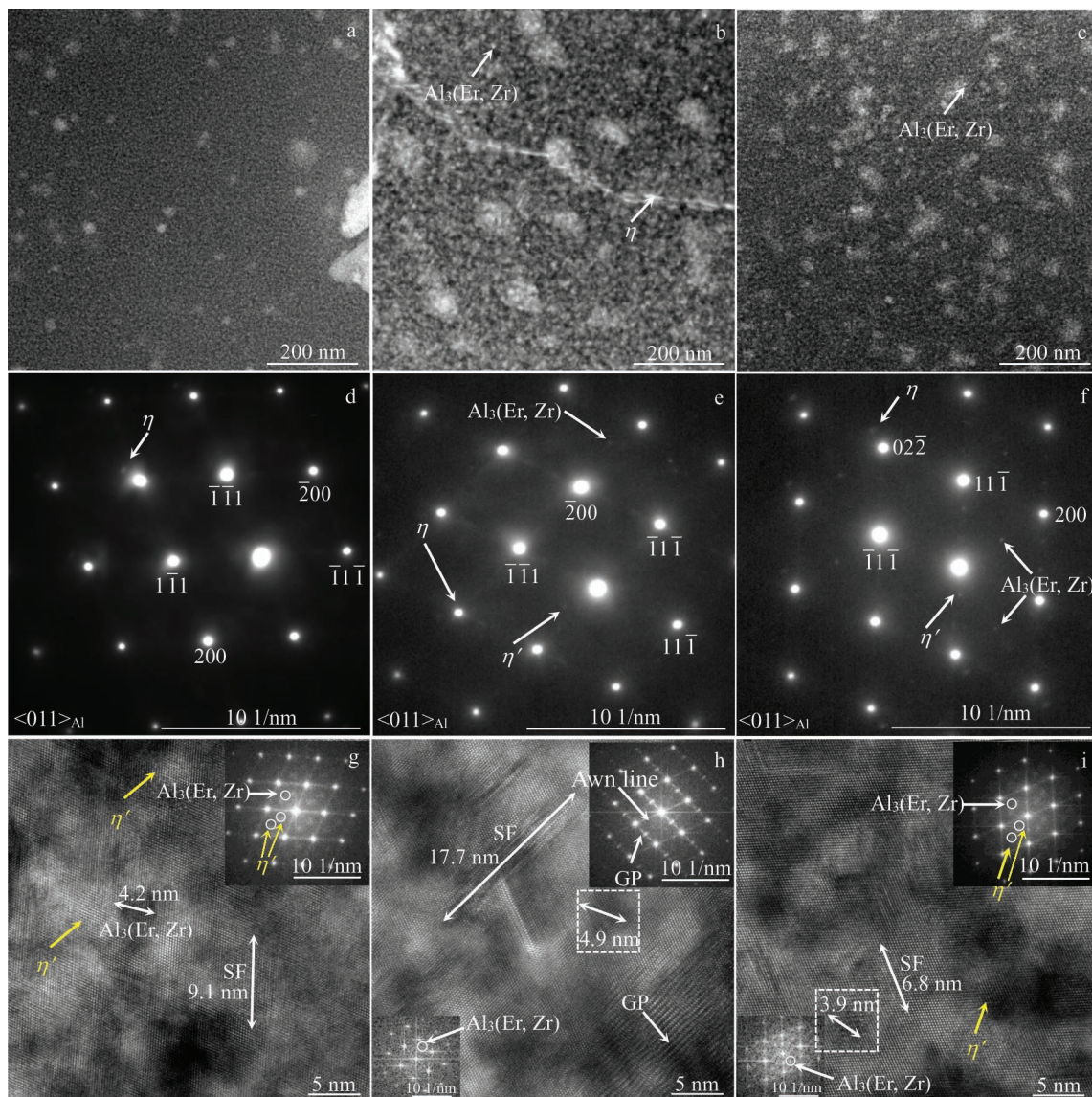


Fig.9 HAADF-STEM morphologies (a~c), SAED patterns (d~f), HRTEM images, and FFT patterns (g~i) of precipitates in Al-7.88Zn-2.05Mg-1.70Cu-0.19Er alloys after peak-aging (a, d, g), over-aging (b, e, h), and double-aging (c, f, i) treatments

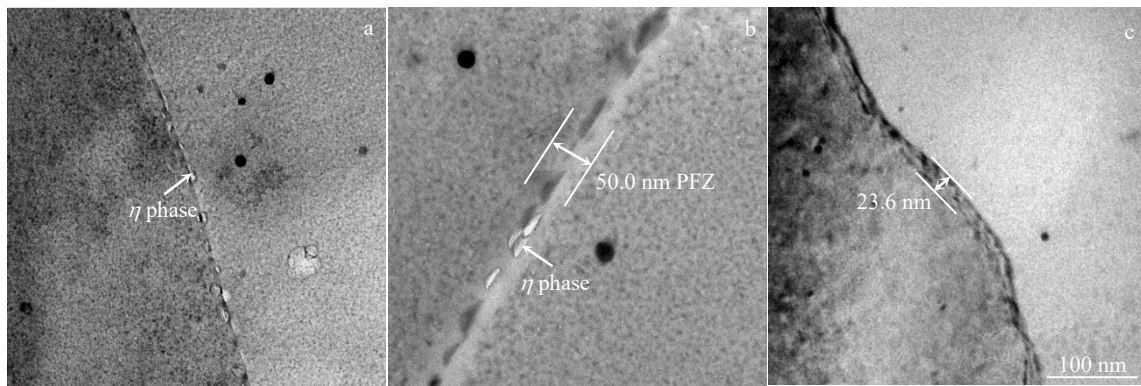


Fig.10 TEM microstructures of GBPs of Al-7.88Zn-2.05Mg-1.70Cu-0.19Er alloys after peak-aging (a), over-aging (b), and double-aging (c) treatments

absorb dislocations, thereby avoiding the stress concentration and improving the plasticity<sup>[26]</sup>.

According to Fig.9c, the precipitates are moderately large in the double-aged alloy specimen, compared with those in peak-aged and over-aged alloys, but the precipitate number density is high. As shown in Fig.9f, the diffraction spots at  $1/2(200)$  with  $1/2(220)$  and  $1/3(111)$  reflect the diffraction features of  $Al_3(Er, Zr)$  and  $\eta'$  phases, respectively. It can be seen that most precipitates are still coherent with Al matrix lattice, and the fine and globular  $Al_3(Er, Zr)$  phase of 3.9 nm in size can be observed. Based on these precipitate characteristics, the double-aged and peak-aged alloys have similar strengths. The width and length of SF in double-aged alloy, about 6.8 nm, are less than those in the over-aged alloy, but the amount of SF is greater. Thus, the plasticity of double-aged alloy is similar to that of over-aged alloy.

GBPs of three alloy specimens are presented in Fig. 10. Fig. 10a shows that GBPs are tiny in the peak-aged alloy specimen and they are mostly distributed as a continuous line. PFZ is too narrow to be observed in Fig.10a. According to the stress corrosion mechanism<sup>[4]</sup>, the corrosion channels are easily formed during the anodic dissolution process. Therefore, the cracks extend along the grain boundary, resulting in the slow strain corrosive fracture of peak-aged alloy specimen. This phenomenon is consistent with the intergranular fracture morphologies in the peak-aged alloy (Fig. 6a and 6b). However, the over-aged alloy specimen shows the opposite results. The precipitates become coarser and accumulate along the grain boundaries. Simultaneously, PFZ of 50.0 nm in width is formed, which may decrease the electron scattering, thereby improving the electrical conductivity. In addition, the coarsened and discontinuous GBPs can decrease the anodic dissolution speed, acting as the entrapping regions for atomic hydrogen ions. The hydrogen bubbles are generated to reduce the accumulation of the hydrogen ions at the grain boundaries<sup>[27]</sup>. Therefore, the over-aged alloy specimen has dimple fracture morphology without intergranular cracks.

The intermediate and discontinuous GBPs are extensively distributed in double-aged alloy specimen, as shown in

Fig. 10c. The size of GBPs in double-aged alloy is less than that in over-aged alloy. Additionally, the width of PFZ in double-aged alloy (23.6 nm) is about half of that in over-aged alloy (50.0 nm). Thus, the corrosion resistance of double-aged alloy specimen is decreased.

### 3 Conclusions

1) The grains of Al-7.88Zn-2.05Mg-1.70Cu-0.19Er alloy after solution treatment at 475 °C for 1 h are lath-shaped, consisting of fine subgrains. The recrystallization area and large-angle grain boundary account for 50.83% and 27.8%, respectively. The average grain size is 15.53  $\mu\text{m}$  in solution-treated alloy.

2) The optimal heat treatment for Al-7.88Zn-2.05Mg-1.70Cu-0.19Er alloy is 475 °C/1 h+120 °C/6 h+150 °C/24 h, namely solution+double-aging treatment. The hardness, ultimate tensile strength, yield strength, and elongation of the alloy after optimal heat treatment are 1859.1 MPa, 669.4 MPa, 624.1 MPa, and 11.2%, respectively. The electrical conductivity, exfoliation corrosion rating, and stress corrosion cracking sensitivity of the alloy after optimal heat treatment are 35.5%IACS, EA, and 4.07%, respectively.

3) After solution+double-aging treatment, the fine spherical  $Al_3(Er, Zr)$  and  $\eta'$  phases are uniformly distributed in the Al matrix, which improves the plasticity, strength, and stress corrosion cracking resistance of the alloy. The fine  $\eta$  precipitates discontinuously distributed in the grain boundaries and wide precipitate free zones can reduce the stress corrosion sensitivity of Al-7.88Zn-2.05Mg-1.70Cu-0.19Er alloy.

### References

- 1 Rometsch P A, Zhang Y, Knight S. *Transactions of Nonferrous Metals Society of China*[J], 2014, 24(7): 2003
- 2 Sigli C. *Materials Science Forum*[J], 2006, 519-521: 321
- 3 Liu Shengdan, Wang Qing, Yang Zhenshen et al. *Materials Characterization*[J], 2019, 156: 109 837
- 4 Rao A C U, Vasu V, Govindaraju M et al. *Transactions of Nonferrous Metals Society of China*[J], 2016, 26(6): 1447

- 5 Song Weiyuan, Lin Gaoyong, Li Qi. *Nonferrous Metals Science and Engineering*[J], 2018, 9(5): 37 (in Chinese)
- 6 Wang Shaohua, Meng Linggang, Yang Shoujie et al. *Transactions of Nonferrous Metals Society of China*[J], 2011, 21(7): 1449
- 7 Bai Song, Huang Tiantian, Xu He et al. *Materials Science and Engineering A*[J], 2019, 766: 138 351
- 8 Wang Yichang, Wu Xiaodong, Cao Lingfei et al. *Materials Science and Engineering A*[J], 2020, 792: 139 807
- 9 Fang H C, Chao H, Chen K H. *Materials Science and Engineering A*[J], 2014, 610: 10
- 10 Shi Weining, Zhou Haifei, Zhang Xinfang. *Acta Metallurgica Sinica (English Letters)*[J], 2020, 33(10): 1379
- 11 Wu H, Wen S P, Huang H et al. *Journal of Alloys and Compounds*[J], 2016, 685: 869
- 12 Wu H, Wen S P, Huang H et al. *Materials Science and Engineering A*[J], 2016, 651: 415
- 13 Xie Peng, Chen Songyi, Chen Kanghua et al. *Corrosion Science* [J], 2019, 161: 108 184
- 14 Pankade S B, Khedekar D S, Gogte C L. *Procedia Manufacturing*[J], 2018, 20: 53
- 15 Zou Yan, Wu Xiaodong, Tang Songbai et al. *Materials Characterization*[J], 2020, 169: 110 610
- 16 Pan Yanlin, Zhang Di, Liu Haoran et al. *Journal of Alloys and Compounds*[J], 2021, 853: 157 199
- 17 Chen Junfeng, Zhang Xingfeng, Zou Linchi et al. *Materials Characterization*[J], 2016, 114: 1
- 18 Sun Yuanwei, Pan Qinglin, Lin Sen et al. *Journal of Materials Research and Technology*[J], 2021, 12: 1303
- 19 Zuo Jinrong, Hou Longgang, Shi Jintao et al. *Journal of Alloys and Compounds*[J], 2017, 716: 220
- 20 Lin Gaoyong, Huang Ting, Zheng Ying. *China Patent*, CN112538599A[P], 2021 (in Chinese)
- 21 Huo Wangtu, Hu Jiangjiang, Cao Huihui et al. *Journal of Alloys and Compounds*[J], 2019, 781: 680
- 22 Zhang Jing, Yang Liang, Zuo Rulin. *Rare Metal Materials & Engineering*[J], 2015, 44(4): 956 (in Chinese)
- 23 Salazar-Guapurich M A, Zhao Y Y, Pitman A et al. *Materials Science Forum*[J], 2006, 519-521: 853
- 24 Özer G, Karaaslan A. *Materials and Corrosion*[J], 2017, 68(11): 1260
- 25 Chakrabarti T, Manna S. *Computational Materials Science*[J], 2018, 154: 84
- 26 Xiao Yunzhen. *Thesis for Master*[D]. Harbin: Harbin Institute of Technology, 2020 (in Chinese)
- 27 Goswami R, Lynch S, Holroyd N J et al. *Metallurgical and Materials Transactions A*[J], 2012, 44(3): 1268

## 超高强铝合金 Al-7.88Zn-2.05Mg-1.70Cu-0.19Er 薄带的组织与性能

黄 婷<sup>1</sup>, 刘会群<sup>1</sup>, 林高用<sup>1</sup>, 郑 英<sup>2</sup>

(1. 中南大学 材料科学与工程学院, 湖南 长沙 410083)

(2. 中南大学 轻合金研究院, 湖南 长沙 410083)

**摘 要:** 研究了超高强冷轧态 Al-7.88Zn-2.05Mg-1.70Cu-0.19Er 合金薄带的组织、力学性能和耐腐蚀性能。结果表明, 对厚度为 0.5 mm 的冷轧态薄带试样进行 475 °C/1 h/水冷固溶处理及 120 °C/6 h+150 °C/24 h 双级时效处理后, 薄带合金具有优良综合性能, 其硬度、极限抗拉伸强度、屈服强度和伸长率分别为 1859.1 MPa、669.4 MPa、624.1 MPa 和 11.2%, 该力学性能与峰值时效态合金的力学性能相当。该状态下合金的电导率、剥落腐蚀等级和应力腐蚀敏感指数分别为 35.5%IACS、EA 和 4.07%。细小的球状 Al<sub>3</sub>(Er, Zr) 和 η' 相均匀分布在 Al 基体中, 且大部分析出物与 Al 基体晶格共格。细小不连续分布的晶界析出 η 相是该合金具有较低应力腐蚀敏感性的主要原因。

**关键词:** Al-7.88Zn-2.05Mg-1.70Cu-0.19Er 合金; 薄带; 双级时效; 力学性能; 耐腐蚀性能

作者简介: 黄 婷, 女, 1997年生, 硕士, 中南大学材料科学与工程学院, 湖南 长沙 410083, E-mail: 1341988001@qq.com